Research Square

Preprints are preliminary reports that have not undergone peer review.
They should not be considered conclusive, used to inform clinical practice,
or referenced by the media as validated information.

Slab stagnation sustained by wet harzburgite and dry basaltic slab assemblages

Danian Shi

shidanian@cags.ac.cn

Chinese Academy of Geological Sciences https://orcid.org/0000-0002-0822-3415

Yang Shen

Graduate School of Oceanography, University of Rhode Island https://orcid.org/0000-0002-4185-6089

Rongtao Zhao

SinoProbe Laboratory, Chinese Academy of Geological Sciences

Jianyu Shi

National Marine Environmental Forecasting Center https://orcid.org/0000-0002-1034-1285

Changxin Chen

Chinese Academy of Geological Sciences

Xiaoming Xu

Institute of Geophysics, China Earthquake Administration

Yongqian Zhang

Chinese Academy of Geological Sciences

Yao Xu

Chinese Academy of Geological Sciences

Hua Xiang

Institute of Geology, Chinese Academy of Geological Sciences https://orcid.org/0000-0001-9221-7132

Yan Liu

Chinese Academy of Geological Sciences

Yan Yang

Chinese Academy of Geological Sciences

Article

Keywords:

Posted Date: October 15th, 2025

DOI: https://doi.org/10.21203/rs.3.rs-7167094/v1

License: This work is licensed under a Creative Commons Attribution 4.0 International License. Read Full License

Additional Declarations: There is **NO** Competing Interest.

Version of Record: A version of this preprint was published at Nature Communications on July 16th, 2026. See the published version at https://doi.org/10.1038/s41467-026-75639-9.

Abstract

Slab stagnation in the mantle transition zone is critical for the mantle dynamics and evolution of Earth’s interior but remains poorly understood1-4. Here we present seismic images that show two key features near Eurasia's northeastern margin: 1) a 700-km-deep, 400-km-wide discontinuity within the slab stagnation zone, matching the akimotoite-bridgmanite transition in an anhydrous basaltic assemblage at adiabatic temperature of ~1000K, and 2) the 660-km discontinuity depressed below the Clapeyron slope of the post-spinel phase transition by ~15 and ~10 km , likely induced by water, respectively in front of the Pacific plate and at the center of the slab stagnation zone. Our mineral physics modeling indicates that the slab stagnation is initiated and sustained predominantly by buoyancy from the excess depressions in the pyrolite and harzburgite mantle and aided by buoyancy of the dry basaltic assemblage in the uppermost lower mantle.

Main

3.1 Hydrochar production and distribution of HMs during HTC process

3.1.1 Hydrochar yield

As shown in Table 1, the yield of hydrochar produced in the water medium was 49.64%, while the introduction of PA resulted in a yield ranging from 37.04% (PAHC-10) to 54.42% (PAHC-40). Increasing the PA dosage from 0.01 wt% to 10 wt% significantly decreased the hydrochar yield from 50.23–37.04%. However, further increasing the dosage to 20 wt% and 40 wt% boosted the yield up to 54.42%, the highest observed. The variation can be attributed to the strong ionization capacity of PA, which releases H^+ ions that accelerate the HTC process. This promotes biomass carbonization and dehydration, while enhancing organic matter breakdown [25, 26], thereby intensifying reactions but reducing solid-phase retention. At higher PA dosages, excess PA also acts as an additional organic substrate, thus increasing hydrochar yield significantly [19]. Furthermore, the ash content of hydrochars declined from 4.87–0.29% (Table 1), which can be explained by the enhanced dissolution of inorganic minerals into the acidified liquid phase [17, 27].

Table 1
The yield of hydrochars and their physicochemical properties

Samples	Yield	N	C	H	S	O	H/C	O/C	Ash	HHV	Total energy
	(%)	(%)	(%)	(%)	(%)	(%)	(%)	(%)	(%)	(MJ/kg)	MJ
WB	--	0.92	44.21	6.05	0.61	42.50	1.64	0.72	5.71	15.99	159.90
WHC	49.64	0.96	57.93	5.75	0.12	31.39	1.19	0.41	3.86	22.17	110.05
PAHC-0.01	50.23	0.98	60.99	5.68	0.09	27.87	1.12	0.34	4.87	23.73	119.20
PAHC-0.25	48.43	1.08	63.46	5.71	0.10	26.01	1.08	0.31	3.09	24.94	120.78
PAHC-0.5	41.66	1.15	66.33	5.27	0.11	26.17	0.95	0.30	0.87	25.25	105.19
PAHC-0.75	40.20	1.19	67.52	5.39	0.14	25.06	0.96	0.28	0.71	26.03	104.64
PAHC-1	40.17	1.13	69.32	5.65	0.11	22.89	0.98	0.25	0.43	27.40	110.07
PAHC-2.5	40.04	1.14	69.03	5.66	0.10	22.95	0.98	0.25	0.20	27.30	109.31
PAHC-5	38.20	0.84	69.08	5.75	0.11	22.71	1.00	0.25	0.66	27.48	104.97
PAHC-10	37.04	0.76	69.48	5.76	0.11	22.06	0.99	0.24	0.49	27.75	102.79
PAHC-20	38.80	0.65	69.44	5.67	0.11	22.91	0.98	0.25	0.23	27.47	106.58
PAHC-40	54.42	0.60	69.4	5.16	0.14	24.14	0.89	0.26	0.29	26.50	144.21

[a] O%= 100% – (C + H + N + S) %

[b] Higher heating value.

3.1.2 Distribution of HMs during the HTC process

The migration and distribution patterns of HMs contained in WB are extremely important for the safety risk assessment of hydrochar. As shown in Fig. 1, 98.65% of Cd and 41.80% of Zn were retained in the solid-phase WHC under water medium condition. However, with the addition of PA to the hydrothermal system, most Cd and Zn were distributed into the liquid phase, and this migration intensified with increasing PA dosage. At a PA concentration of 0.75 wt%, 99.61% of Cd and 92.45% of Zn were removed from the solid phase, and when the concentration increased to 5 wt%, only 0.05% of Cd and 0.35% of Zn remained in the hydrochar, suggesting a near-complete transfer of these metals to the liquid phase. This effect results from the acidification of the solution by proton ionization from PA, which promotes both the dissociation of HMs from solid substrates and the hydrolysis of biomass, generating organic acids [28]. These organic acids further form soluble complexes with HMs, facilitating their migration into the liquid phase [17]. It was

observed that 0.75 wt% PA can dissolve more than 99% of Cd from the solid phase, and 5 wt% PA can make Zn reach the same level (Fig. 1). It is due to the relatively high initial content of than that of Cd in WB which need more PA to release Zn. Additionally, Zn often combines with structural components such as cell walls to form a relatively stable complex or deposition form, which also inhibits its migration. The studies show most Cd accumulates in plant cells as organic acid complexes and is unstable [29]). Therefore, under the catalysis of PA, Cd is more easily transferred to the liquid phase than Zn [30].

Figure S1 shows the concentrations of HMs in WB and the resulting WHC. The initial contents of Cd and Zn in WB were 71.89 mg/kg and 736.26 mg/kg, respectively, indicating a high ecological risk. After HTC, the concentrations of Cd and Zn in WHC increased to 129.65 mg/kg and 798.34 mg/kg, respectively. This increase is mainly attributed to the low volatility and high thermal stability of most HMs under HTC conditions, which retain them in the solid phase. The decomposition of organic matter (primarily hemicellulose and cellulose) during HTC results in a carbon concentration effect, further elevating the HMs content. Thus, although HTC effectively reduces biomass volume and may stabilize certain metal species, the elevated concentrations of HMs in WHC still pose potential ecological risks. However, the addition of PA led to a reduction in Cd and Zn concentrations in all PAHCs, except PAHC-0.01. According to the NY/T4159-2022 standard, the use of biochar in agriculture is categorized as Level I or II, based on the degree of carbonization and pollutant content. As shown in Table S1, when the PA concentration exceeds 0.5 wt%, the resulting PAHC meets the Grade II biochar standard, allowing its use in fields or as fertilizer under compliance requirements. PAHC produced at 5 wt% PA meets the Grade I standard, enabling its application directly in agriculture. In summary, the addition of PA during HTC of HMs-contaminated woody biomass facilitates metal migration, reduces the metal content in hydrochars, and mitigates associated environmental risks.

3.2 Hydrochars Structure and surface properties

3.2.1 Hydrochars composition

Figure 2(a) shows the digital photographs of WB and hydrochars. With increasing PA concentration, the color of PAHC changes from brown to black, accompanied by an increase in carbon content from 44.21% (RM) to 57.93% (WHC) and 69.48% (PAHC-40). (Table 1). These changes in color and carbon content are attributed to the catalytic effect of PA on the hydrothermal polymerization and carbonization processes of cellulose, hemicellulose, and lignin, thereby enhancing the material's aromaticity and carbon retention [31]. When the PA concentration exceeds 10 wt%, the carbon content stabilizes at approximately 69.4%, indicating that the reaction has reached equilibrium and a stable carbon structure has formed [32].

The O content in PAHC initially decreases (from 27.87–22.06%) and then slightly increases (to 24.14%) (Table 1). At low levels of PA ranged from 0.1 to 10 wt%, protons (H^+) facilitate decarboxylation and dehydration reactions, thereby reducing oxygen content [33]. At higher PA levels (20–40 wt%), more phosphate groups may be incorporated into the solid phase, accounting for the slight increase in oxygen content. The nitrogen content exhibits an initial increase followed by a decrease, which is likely due to the Maillard reaction under hydrothermal conditions that produces nitrogenous heterocycles retained in the solid phase. However, excessive PA can promote the transformation of organic nitrogen into soluble NH_4^+-N,

thereby reducing nitrogen retention in PAHC [34, 35]. The H/C and O/C ratios (Table 1) decrease with increasing PA content, indicating a higher degree of carbonization, increased aromaticity, and improved structural stability [36]. The Van Krevelen diagram (Fig. 2(b)) further confirms that PA facilitates both dehydration and decarboxylation, which are key pathways in HTC [37]. At 40 wt% PA, a shift in the reaction mechanism is observed, potentially due to the abundance of phosphate groups, leading to a relative increase in oxygen content [38].

3.2.2 Surface properties

The crystalline and chemical structures of PAHC were analyzed using XRD, FTIR, and XPS. As shown in Fig. 2c, the XRD pattern of WHC exhibits distinct diffraction peaks at 15°, 22.4°, and 24.4°, corresponding to cellulose I, cellulose II, and calcium carbonate, respectively [25]. With increasing PA concentration, the intensities of these characteristic cellulose peaks progressively diminish and eventually vanish at 0.5–0.75 wt% PA, indicating the destruction of the crystalline cellulose structure. Simultaneously, broad peaks emerge in the 19°–21° range, indicative of amorphous carbon formation, likely due to the isomerization, depolymerization, and polymerization of cellulose-derived monosaccharides into carbonaceous clusters [38]. Additionally, the 24.4° peak corresponding to calcium carbonate disappears, and new peaks at 28°, 30°, and 34° emerge in PAHC-0.01 and PAHC-0.25, which are identified as calcium phosphate salts (ICSD 98-041-0782) using High-Score Plus software. However, further increases in PA result in the disappearance of calcium phosphate peaks, which can be attributed to their dissolution by excess protons, consistent with SEM observations. Notably, at 0.01 wt% PA, PAHC's ash content briefly surpassed WHC's (Table 2), potentially from calcium phosphate precipitation between Ca^{2+} and phosphate ions [19, 39]. Beyond 0.25 wt%, excessive proton release leads to further phosphate salt dissolution and reduced ash content.

Table 2
The specific surface area and pore structure of WB and hydrochars in different media

Samples	SSA	Total pore volume	Mean pore diameter
	[m^2/g]	[cm^3/g]	[nm]
WB	2.78	0.01	10.38
WHC	8.65	0.03	13.23
PAHC-0.01	7.12	0.04	19.70
PAHC-0.25	8.86	0.05	23.63
PAHC-0.5	9.94	0.08	33.86
PAHC-0.75	9.79	0.09	35.90
PAHC-1	11.12	0.09	30.68
PAHC-2.5	11.31	0.09	30.91
PAHC-5	12.14	0.11	36.28
PAHC-10	10.18	0.09	35.21
PAHC-20	13.53	0.08	24.00
PAHC-40	13.59	0.07	21.85

XPS analysis (Fig. S5-S7) reveals that the surface elemental composition of PAHC varies with PA dosage: C (73.3–81.92%), O (0.65–1.09%), and P (17.11–22.72%). Increasing PA enhances the C1s peak while decreasing O1s, reflecting greater dehydration, decarboxylation, and carbonization. Deconvolution of the C1s spectrum shows variations in C–C (284.8 eV), C–O (286.0 eV), and C = O (289.0 eV) [40]. Initially, C–C increases and then declines, while C–O and C = O exhibit inverse trend, attributed to hydroxyl group removal and polymerization-induced double bond formation. Phosphorus content shows a non-linear trend: initially present (0.16%) in PAHC-0.01 due to intrinsic phytate phosphorus, then decreasing as PA hydrolyzes it to inositol and orthophosphoric acid [41], and finally rising again at higher PA dosages (e.g., PAHC-40 at 0.2%) due to phosphate adsorption and incorporation [42, 43]. This observation verifies phosphorus' dual transformation pathway: biomass-derived release coupled with PA-mediated phosphate re-association.

FTIR analysis (Fig. 2d) further elucidated the evolution of surface functional groups. Notable absorption bands at 3343 and 3372 cm^{-1} (–OH stretching), and at 2853, 2922, and 1456 cm^{-1} ($–CH_2$ stretching) were observed [44, 45], whose intensities diminished with increasing PA concentration. This phenomenon indicates the degradation of hydroxyl groups and aliphatic chains during HTC, facilitating the formation of aromatic structures [46, 47]. Aromaticity was supported by increased intensities at 1513 cm^{-1} and 1610 cm^{-1}, corresponding to C = O/C = C bonds, due to enhanced H^+-catalyzed aromatization [20, 48]. Simultaneously, the C–O stretching peak at 1032 cm^{-1} weakened, suggesting ketone–enol tautomerism and molecular rearrangement [49]. Rising PA concentrations diminish P = O signals from phosphate bonds while enhancing phosphate group signals, indicating dual mechanisms: (1) PA-catalyzed biomass decomposition

releases intrinsic phosphates into the liquid phase, and (2) hydrothermal incorporation of phosphate groups onto PAHC surfaces at elevated PA levels. In addition, XRD shows that phosphate groups in the liquid phase may produce metal precipitation, which increases P = O of the phosphate group [50, 51].

3.2.3 Structure properties

As shown in Fig. S2, the raw material primarily consists of elongated strips and rough particles, with embedded white material identified as calcium carbonate [15]. Figure 2(e–n) demonstrate that PA catalysis induces significant fragmentation of the hydrochar, forming deep ravines and large pores as a result of calcium carbonate dissolution, thereby increasing surface roughness. Carbon microspheres and clusters are also observed, with both their size and abundance increasing at higher PA concentrations. These features are attributed to the acid-catalyzed hydrolysis of biomass components into oligosaccharides, hexoses, and lignin fragments, followed by subsequent dehydration and polymerization reactions [26, 52].

Such surface morphological transformations directly influence adsorption performance, as verified by N_2 adsorption–desorption analysis. As shown in Table 2, PAHC-40 exhibits the highest specific surface area (SSA_{BET}) of 13.59 m²/g, representing a 90.87% increase compared to PAHC-0.01. The enhancement is attributed to ash removal, carbon microsphere formation, and biomass decomposition [20]. However, the total pore volume and average pore diameter initially increase and then decrease, likely due to microsphere aggregation and pore blockage under high PA loading, as shown in Fig. 2(e–n) [31, 38]. BJH pore size analysis (Fig. S3–S4) shows H_3-type hysteresis loops, indicating dominant microporosity [53]. As PA increases, smaller pores (< 10 nm) diminish, and the dominant pore size shifts from mesopores (16.97–42.02 nm at 0.25–2.5 wt%) to macropores (52.64–55.29 nm at 5–20 wt%). Notably, PAHC-0.01 has a peak diameter of 56.51 nm due to calcium carbonate dissolution, while PAHC-40's 31.33 nm peak suggests pore blockage by carbon microspheres and the presence of additional micropores during the averaging calculation process. Thus, moderate PA (0.5–10 wt%) promotes HTC, enhancing porosity and SSA, whereas excessive PA (20–40 wt%) leads to pore obstruction and structural collapse due to over-catalysis [20].

(Note: a: cellulose I, b: cellulose II, c: calcium carbonate, d: calcium phosphate salt, e: amorphous carbon, f: calcium phosphate)

3.2.4 Thermal stability and fuel traits

TG-DTG analysis revealed three distinct combustion stages for WB and the hydrochars obtained at different PA concentrations: (1) moisture evaporation, (2) volatile combustion associated with cellulose and hemicellulose degradation, and (3) oxidation of fixed carbon [54]. As illustrated in Fig. S8, WB exhibits weight loss peaks at 77°C, 330°C, and 460°C, corresponding to the evaporation of moisture, the decomposition of cellulose and hemicellulose, and the formation of stable carbonaceous structures, respectively. Following HTC, the thermal behavior of PAHC underwent substantial alterations. Dehydration and carbonization reactions during HTC, facilitated by the catalytic role of PA, reduced the moisture content in PAHC, resulting in lower initial-stage weight loss. In the second stage, sharper peaks were observed for PAHC-0.01 and PAHC-0.25, indicating a notable reduction in cellulose and hemicellulose components. At higher PA concentrations (PAHC-0.5 and PAHC-0.75), the peaks in the second combustion stage became broader and more complex, shifting from 320°C to 380°C, suggesting the generation of new intermediate

structures and improved thermal resistance. These trends were corroborated by elemental analysis, XRD, and FTIR results, which demonstrate progressive aromatization with increasing PA concentration [54, 55].

Such structural transformation not only enhances the thermal stability of PAHC but also significantly improves its fuel characteristics. It has been confirmed that increasing PA concentration facilitates the transfer of most HMs into the liquid phase, thereby rendering PAHC produced under PA catalysis a promising candidate for high-quality, clean fuel. The calorific value of PAHC increases from 22.17 MJ/kg to 27.47 MJ/kg with rising PA concentrations (Table 1), comparable to that of lignite (23.95 MJ/kg) [56]. Additionally, the sulfur content of PAHC ranges from 0.09–0.14% (Table 1), qualifying it as an S-L1–L3 grade clean fuel (Std = 0–0.75%) according to the "Classification of Coal Product Variety" standard in China (GB17608-2022) [57].

3.3 Adsorption capacity of hydrochars to solution HMs

3.3.1 Batch adsorption experiments

To evaluate the environmental applicability of hydrochar, a series of batch adsorption experiments were performed to assess the HMs removal capacities of WHC and PAHC. As shown in Fig. 3(a–b), PAHC exhibited superior adsorption performance for both Cd^{2+} and Cu^{2+} among those biochars. Specifically, as the PA level increased from 0.01 wt% to 40 wt%, the adsorption amount of Cd^{2+} and Cu^{2+} by PAHC ranged from 1.88 ± 0.05 mg/g to 6.40 ± 0.47 mg/g and 5.55 ± 0.31 mg/g to 15.30 ± 0.06 mg/g, respectively, representing 1.20–4.08 times and 1.16–3.18 times higher adsorption than WHC. This is mainly attributed to the more abundant surface functional groups (e.g., C, O, and P groups) in PAHC, which play a dominant role in the adsorption of HMs. In addition, the relatively high SSA of PAHC may enhance the overall adsorption capacity by providing additional contact sites. Interestingly, as the PA dosage increased, the adsorption of Cd^{2+} and Cu^{2+} on PAHC initially decreased and then increased, a trend that did not correspond directly with the observed variations in pore structure, mineral composition, and active functional groups of PAHC. Previous studies have indicated that at low PA concentrations (0.01–0.25 wt%), phosphate groups derived from biomass can chelate with HMs to form polymeric precipitates through multi-element interactions, thereby enhancing adsorption [26, 48]. However, as the PA concentration rises to 0.5–1 wt%, the increased concentration of ionized protons may inhibit the formation of HMs precipitates [17] Additionally, H^+ ions may accelerate the dissolution of inorganic salts in the biomass, thereby reducing the ion exchange capacity of the hydrochar [58]. Nevertheless, when the PA addition increases to 2.5–40 wt%, the significantly enlarged SSA and abundant phosphate functional groups of PAHC become the dominant factors contributing to HMs adsorption [21, 59].

3.3.2 The effect of solution pH on adsorption

The pH significantly affects both the adsorbent's surface charge and the speciation of metal ions in solution. As illustrated in Fig. 3(c–d), the adsorption capacities of Cd^{2+} and Cu^{2+} onto hydrochars gradually increase as the pH rises from 2.0 to 5.0. During this range, WHC exhibits a higher adsorption capacity than PAHC. As the pH increases from 5.0 to 7.0, the adsorption capacities for both metals rise more sharply, with PAHC outperforming WHC. At pH ≥ 8, adsorption reaches equilibrium. This trend corresponds to changes in the zero point of charge (ZPC) of PAHC (Fig. S9). Increasing the amount of PA during hydrochar preparation

shifts the ZPC to the left, resulting in a more negatively charged surface. The greater surface negativity enhances electrostatic attraction between PAHC and the positively charged Cd^{2+} and Cu^{2+}, thereby increasing metal adsorption [59, 60]. As shown in Fig. S10, the speciation of Cd(II) and Cu(II) in aqueous solution was simulated and calculated using Visual MINTEQ 3.1 software [61]. At pH < 5, the dominant species are Cd^{2+} and Cu^{2+}. Under these conditions, protonation of hydrochar surfaces leads to positively charged sites, which generate electrostatic repulsion with metal cations, thereby inhibiting adsorption. Between pH 5 and 7, the deprotonation of surface functional groups enhances their complexation capabilities, improving adsorption efficiency. At higher pH, metal ions begin to form insoluble hydroxide precipitates (e.g., $Cd(OH)_2$ and $Cu(OH)_2$), which are removed from the aqueous phase via precipitation rather than by adsorption [62, 63]. Notably, PAHC-40 exhibits enhanced adsorption even at low pH due to its lower ZPC and increased deprotonation capacity, which intensify the surface's negative charge and thus strengthen the electrostatic attraction to metal ions.

3.3.3 Adsorption isotherm and kinetics

Figure 4(a–b) shows that the adsorption isotherms of Cd^{2+} and Cu^{2+} on hydrochars exhibit typical L-shaped curves, indicating favorable and homogeneous adsorption processes [64, 65]. The Langmuir and Freundlich isotherm models were applied to analyze the adsorption data, with corresponding curves and fitting parameters presented in Fig. 4(a–b) and Table 3. For Cd^{2+} adsorption onto WHC, PAHC-0.75, PAHC-5, PAHC-20, and PAHC-40, the correlation coefficients (R^2) for the Langmuir model are 0.9501, 0.9642, 0.9672, 0.9672, and 0.9715, respectively, all higher than those of the Freundlich model (Table 3). The results suggest that Cd^{2+} adsorption by hydrochars follows a monolayer adsorption mechanism, dominated by chemisorption [66, 67]. In contrast, the adsorption isotherm data for Cu^{2+} on PAHCs (excluding WHC) fit well with both the Langmuir and Freundlich models, suggesting a combination of chemical and physical adsorption mechanisms. The WHC, with relatively undeveloped pore structure and lower SSA compared to PAHCs, relies more on chemical adsorption processes, such as complexation and ion exchange, which enhance HMs affinity despite limited SSA [15]. Furthermore, Langmuir model fitting reveals that PAHC-40 exhibits the highest adsorption capacities for Cd^{2+} and Cu^{2+}, with Q_{max} values of 13.59 mg/g and 63.59 mg/g, respectively.

Table 3
The isotherm parameters of Cd^{2+} and Cu^{2+} adsorption by hydrochars

Samples	HMs	Langmuir model parameters			Freundlich model parameters		
		K_L	q_{max}	R^2	K_F	n	R^2
WHC	Cd^{2+}	0.139	6.30	0.9501	1.41	0.34	0.8100
	Cu^{2+}	0.026	19.13	0.9509	1.02	0.58	0.9011
PAHC-0.75	Cd^{2+}	0.070	10.84	0.9642	1.56	0.41	0.8705
	Cu^{2+}	0.028	23.88	0.9679	1.40	0.58	0.9676
PAHC-5	Cd^{2+}	0.059	12.67	0.9672	1.57	0.44	0.8870
	Cu^{2+}	0.024	27.72	0.9850	1.36	0.60	0.9750
PAHC-20	Cd^{2+}	0.059	12.67	0.9672	1.57	0.44	0.8870
	Cu^{2+}	0.012	57.13	0.9914	1.09	0.75	0.9817
PAHC-40	Cd^{2+}	0.058	13.59	0.9715	1.65	0.44	0.8890
	Cu^{2+}	0.140	63.59	0.9936	1.57	0.72	0.9892

Adsorption kinetics were further investigated to elucidate the adsorption mechanisms, reaction pathways, and rates [7]. The adsorption behavior of Cd^{2+} and Cu^{2+} was modeled using Pseudo -first-order and Pseudo-second kinetic equations, with fitting curves shown in Fig. 4(c–f) and parameters listed in Table S2. As depicted in Fig. 4(c–f), WHC and PAHC both exhibit rapid initial adsorption of Cd^{2+} and Cu^{2+}, followed by a gradual approach to equilibrium. The rapid uptake at the early stage is attributed to the abundant active sites on PAHC and the high initial concentration of metal ions, which promote fast surface binding. In the later stages, the adsorption rate slows down, likely due to intraparticle diffusion limitations [68]. The Cd^{2+} and Cu^{2+} reach equilibrium on WHC after 800 min and 240 min, respectively, while PAHC achieves equilibrium much faster—within 240 min for Cd^{2+} and 60 min for Cu^{2+}. This acceleration is mainly due to the presence of abundant functional groups on PAHC, which show a strong affinity for HMs and enable faster complexation [20]. The Pseudo-second kinetic model provides the best fit for both metals (R^2 >0.99, Table S2), indicating that chemisorption involving electron sharing or exchange is the rate-limiting step [61]. Nonetheless, the Pseudo -first-order model also fits reasonably well (R^2 = 0.929–0.995), implying that physical adsorption mechanisms such as pore-filling and electrostatic interactions also contribute to the overall adsorption process [3]. The Pseudo-second kinetic model (R^2>0.99, Table S2) better fitted HM adsorption data than the first-order model, suggesting rate-limiting chemical adsorption involving electron exchange [61]. The adsorption of Cd^{2+} and Cu^{2+} on hydrochars is mainly controlled by chemical adsorption.

3.3.4 Adsorption mechanisms

As shown in Fig. S11, SEM-mapping images demonstrate that, after adsorption, Cd^{2+} and Cu^{2+} are uniformly distributed across the hydrochar surface, as indicated by the red mapping regions. The distribution intensity follows the order: PAHC-40 > PAHC-0.75 > WHC, indicating a significantly enhanced adsorption capacity in PA-modified hydrochars.

FTIR spectra further support the involvement of functional groups in the adsorption process (Fig. 5a–b). After adsorption, the broad hydroxyl band shifts to 3201–3346 cm^{-1}, suggesting interactions with metal ions. Additional shifts and reductions in intensity were observed for aromatic C = C (1610 cm^{-1}), C = O (1703 cm^{-1}), and –COO (1459 cm^{-1}) groups, implying that complexation occurs between the metal ions and surface functional groups, including hydroxyl, carboxyl, and π-conjugated aromatic systems. Notably, PAHC-40 exhibits pronounced changes in phosphate-related peaks (1215–1283 cm^{-1}), suggesting that P = O and P–O–C bonds play a crucial role in Cd^{2+} and Cu^{2+} binding [69]. Additional peak shifts at 800 and 858 cm^{-1} (P–OH and P–O–C) further support the role of phosphate groups in HMs removal [26].

XRD analysis (Fig. 5c–d) revealed no distinct crystalline peaks corresponding to Cd^{2+} or Cu^{2+} precipitates, suggesting that HMs removal was primarily driven by chemical adsorption and ion exchange rather than precipitation. A slight shift and reduced intensity at 22.3° after adsorption indicate changes in the hydrochar microstructure, likely due to interactions between the hydrochar matrix and metal ions. XPS analysis (Fig. 6) provides additional confirmation of successful metal adsorption. Characteristic peaks of Cd 3d (405.10 eV) and Cu 2p (935.24 eV) were detected in PAHC-0.75 and PAHC-40 [70], confirming the presence of Cd^{2+} and Cu^{2+} on the hydrochar surface. High-resolution C 1s and O 1s spectra revealed changes in the proportions of C = O, C–O, and O–C/O–P bonds after adsorption. In PAHC-40, for example, the peak area of O–C/O–P bonds decreased by 7.32–15.54%, suggesting the participation of these oxygen-containing groups in metal binding [43].

Collectively, the primary adsorption mechanisms for HMs on hydrochar include physical adsorption, ion exchange, and chemical complexation etc. (Fig. 7). Additionally, phosphate groups in PAHC-40 may facilitate co-precipitation with HMs, further enhancing removal efficiency.

Figure 6 The XPS (a, b) of hydrochar before and after adsorption and peak splits of C1s (c, d) and O1s (e, f)

3.4. Hydrochars capacity in HMs immobilization in soil

3.4.1 The physio-chemical properties of soil

The hydrochar at application rates of 1–3% significantly reduced soil bulk density (Fig S12b). Notably, PAHC-treated soils exhibited slightly lower bulk densities (0.79–0.85 $g \cdot cm^{-3}$) compared to WHC-treated soils (0.82–0.85 $g \cdot cm^{-3}$). The result is likely due to the well-developed pore structure of PAHC, which enhances soil looseness and reduces compaction. Correspondingly, soil porosity was notably improved with the addition of PAHC, especially at the 3% level, where porosity increased to 68.03–70.10% (Fig. S12(c)). The higher porosity observed in PAHC-amended soils is mainly attributed to the enhanced internal pore structure of PAHC, which improves soil aeration and water permeability. The cation exchange capacity (CEC) decreased slightly with increasing WHC dosage (95.70–100.28 $cmol \cdot kg^{-1}$), whereas it increased significantly with PAHC (97.61–102.57 $cmol \cdot kg^{-1}$) (Fig. S12(d)). It is likely due to the higher abundance of oxygen-

containing functional groups (e.g., carboxyl and phenolic groups), larger SSA and porous structure in PAHC, which facilitate cation binding or ion exchange compared with WHC.

3.4.2 The chemical speciation of HMs in soil

Hydrochars favorable pore structure and high oxygen concentration enable effective adsorption and immobilization of HMs [43]. As shown in Fig. 8(a) and (c), the percentage of Cd and Zn in CK soil increased during the first week of the WHC-1% and PAHC-1% treatments. The Cd proportion rose in weak AS and OX, from 80.8–82.92% and 81.17%, while the Zn proportion rose from 30.25–34.07% and 31.90%, respectively. The result may be attributed to the release of enriched Cd and Zn from WHC and PAHC-0.75 into the soil, which was not effectively stabilized by lower hydrochar addition. The WHC-3% and PAHC-3% reduced the proportions of AS and OX Cd and Zn in the soil, where Cd were reduced to 78.93% and 78.13%, Zn 28.22% and 27.04%, respectively. The findings suggest that an increase the hydrochar addition results in more effective reduction of the AS and OX of Cd and Zn in soil, and the PAHC has greater stabilization ability than WHC due to its bigger SSA and more oxygen/phosphorus -containing groups.

Figure 8(b) and (d) reveal that by 10th week, the AS fractions of Cd and Zn in CK displayed a significant increase, whereas soils amended with 3% WHC and 3% PAHC showed reductions of 21.24–21.84% and 7.62–8.14%, respectively. Concurrently, the RES fractions of Cd and Zn rose to 10.72–11.80% and 63.91–67.29%, respectively. This observation suggests that hydrochar effectively facilitates the transformation of HMs from labile, weakly acid-soluble/exchangeable forms to stabilized oxidizable and residual phases with prolonged cultivation duration.

3.4.3 Bioavailability of HMs

Figure 8(e–f) illustrates the impact of WHC and PAHC on the bioavailable concentrations of Cd and Zn in soil. In CK soil, the bioavailable contents of Cd and Zn remained relatively stable during the 10-week period, indicating only minor fluctuations without significant changes. In contrast, bioavailable Cd and Zn in WHC-amended soil showed an initial decline before rebounding during the experimental period. By the 10th week, the bioavailable contents of Cd and Zn had increased to 18.34–18.42 mg/kg and 127.58–127.82 mg/kg, respectively. This can be attributed to the initial immobilization of Cd and Zn on the surface of the WHC, which later dissolved and released into the soil. Additionally, PAHC-amended soil exhibited a sustained reduction in Cd/Zn bioavailability throughout cultivation, indicating superior HM stabilization compared to WHC.

3.5 Risk assessment of hydrochars in soil remediation

The potential ecological risk index method was used to evaluate the ecological and environmental effects of HMs in soil following the addition of hydrochar [71]. As shown in Table 4, the concentrations of Cd and Zn in the E_r from all soil types fell below the standard minimum values (≤ 40) after 10th weeks of soil cultivation, indicating the presence of a minor environmental hazard. The C_f index indicates that the overall level of Cd contamination in CK soil is classified as moderate pollution, with a significant ecological risk. The addition of WHC and PAHC resulted in a decrease in the C_f of Cd in the contaminated soil to a range of 7.48–8.33. As demonstrated in Table S4, apart from the 3% WHC sample, the remaining soil samples exhibited indications

of mild contamination. The results manifested that the incorporation of hydrochar can effectively mitigate the pollution levels in HMs soil. After adding hydrochar, the E_r of Cd in the soil diminished from 300.86 to a range of 224.28–249.87, indicative of a 16.95–25.45% reduction. In particular, adding PAHC to soil has been demonstrated to be an effective method for reducing the E_r in contaminated soil. This phenomenon is attributed to the rich pore structure of PAHC and the highly immobilization efficiency of HMs by the oxygen/phosphate-containing groups. The WHC-3% has a higher Er than the WHC-1% due to the release of HMs during soil remediation. The E_r range for all soils is between 160 and 320, which is still a significant ecological hazard. The RI shows significant ecological risk in CK soil, 224.81–250.44 in hydrochar-amended soil, indicating moderate risk. Therefore, hydrochar can effectively reduce the ecological pollution index in HMs-contaminated soil, especially assisting with PAHC is an effective strategy for mitigating potential ecological risks.

Table 4
Ecological risk index of soil amended with different hydrochar

Ecological risk index	CK	WHC-1%	WHC-3%	PAHC-1%	PAHC-3%
$C_{f\ (}$Cd)	10.03	7.87	8.33	7.48	7.48
$E_{r(}$Cd)	300.86	236.18	249.87	224.45	224.28
$C_{f(}$Zn)	0.62	0.52	0.56	0.49	0.52
$E_{r(}$Zn)	0.62	0.52	0.56	0.49	0.52
RI	301.48	236.70	250.44	224.94	224.81

Declarations

Author contributions:

D.S. and Y.S. conducted the study, performed the seismological analysis and wrote the paper. D.S., R.Z. and J.S. performed the data processing. D.S. and H.X. performed the mineral physics modeling. All others contributed to the data collection and improvement of the manuscript.

Competing interests

Authors declare that they have no competing interests.

Acknowledgments

This study was supported by the National Natural Science Foundation of China (grant number 42174109), the National Key Research and Development Program of China (grant number 2016YFC0600201), the China Geological Survey (grant number DD20221829), the National Natural Science Foundation of China (grant number 42174169) and the U.S. Natural Science Foundation (grant number 1927133). We thank the DMCs

of China National Seismic Network at Institute of Geophysics, China Earthquake Administration for providing us the seismic waveform data.

Data availability

All the receiver function data obtained in this study are available from Figshare ###. The receiver function data from the NECsaids and NECESS arrays are available from World Data System for Geophysics at ftp://159.226.119.161/data/NECsaids/RF2020. Raw seismic waveform data from CDSN and CHINArray are available from the DMCs of China National Seismic Network at Institute of Geophysics, China Earthquake Administration (http://www.seisdmc.ac.cn, http://www.chinarraydmc.cn, registration is required to download the data). Raw waveform data from the stations of the WDSN and the northeastern Tibet seismic experiments are available from the IRIS DMC (http://ds.iris.edu/ds/nodes/dmc).

Code availability

The seismic ray tracing program used in the construction of the RF images is available at http://geodynamics.org/cig/software/packages. The thermodynamic code Perple X used for mineral physics modeling is available at https://www.perplex.ethz.ch. All the specific data processing codes and scripts are available from the corresponding authors.

References

1. Gaherty JB, Hager BH (1994) Compositional vs. thermal buoyancy and the evolution of subducted lithosphere. Geophys Res Lett 21:141–144
2. Litasov KD, Ohtani E, Sano A (2006) Influence of water on major phase transitions in the earth's mantle. Geophys Monogr Ser 168:95–111
3. Goes S, Agrusta R, Hunen JV, Garel F (2017) Subduction-transition zone interaction: a review. Geosphere 13(3):1–21
4. Chanyshev A, Ishii T, Bondar D, Bhat S, Kim EJ, Farla R, Nishida K, Liu Z, Wang L, Nakajima A, Yan B, Tang H, Chen Z, Higo Y, Tange Y, Katsura T (2022) Depressed 660-km discontinuity caused by akimotoite–bridgmanite transition. Nature 601:69–73
5. Li C, van der Hilst RD, Engdahl ER, Burdick S (2008) A new global model for P wave speed variations in Earth’s mantle. Geochem Geophys Geosyst 9:Q05018
6. Fukao Y, Obayashi M (2013) Subducted slabs stagnant above, penetrating through, and trapped below the 660 km discontinuity. J Geophys Res 118:5920–5938
7. Ringwood AE, Irifune T (1988) Nature of the 650 km seismic discontinuity: Implications for mantle dynamics and differentiation. Nature 331:131–136
8. Dong J, Fischer RA, Stixrude LP, Brennan MC, Daviau K, Suer TA, Turner KM, Meng Y, Prakapenka VB (2025) Nonlinearity of the post-spinel transition and its expression in slabs and plumes worldwide. Nat Commun 16:1039

9. Ishii T, Frost DJ, Kim EJ, Chanyshev A, Nishida K, Wang B, Ban R, Xu J, Liu J, Su X, Higo Y, Tange Y, Mao H, Katsura T (2023) Buoyancy of slabs and plumes enhanced by curved post-garnet phase boundary. Nat Geosci 16:828–832
10. Isacks B, Molnar P (1971) Distribution of stresses in the descending lithosphere from a global survey of focal mechanism solutions of mantle earthquakes. Rev Geophys 9:103–174
11. Torii Y, Yoshioka S (2007) Physical conditions producing slab stagnation: constraints of the Clapeyron slope, mantle viscosity, trench retreat, and dip angles. Tectonophysics 445:200–209
12. Hirose K, Fei Y, Ma Y, Mao HK (1999) The fate of subducted basaltic crust in the Earth's lower mantle. Nature 397:53–56
13. Kesson SE, Gerald JF, Shelley J (1994) Mineral chemistry and density of subducted basaltic crust at lower-mantle pressures. Nature 372:767–769
14. Ringwood AE (1994) Role of the transition zone and 660 km discontinuity in mantle dynamics. Phys Earth Planet Inter 86:5–24
15. van Keken P, Karato S, Yuen D (1996) Rheological control of oceanic crust separation in the transition zone. Geophys Res Lett 23:1821–1824
16. Wang X, Chen Q, Niu F, Wei S, Ning J, Li J, Wang W, Buchen J, Liu L (2020) Distinct slab interfaces imaged within the mantle transition zone. Nat Geosci 13:822–827
17. Liu C, Banerjee R, Grand SP, Sandvol E, Mitra S, Liang X, Wei S (2024) A high-resolution seismic velocity model for East Asia using full-waveform tomography: Constraints on India-Asia collisional tectonics. Earth Planet Sci Lett 639
18. Li C, van der Hilst RD (2010) Structure of the upper mantle and transition zone beneath Southeast Asia from traveltime tomography. J Geophys Res 115:B07308
19. Simmons NA, Gurrola H (2000) Multiple seismic discontinuities near the base of the transition zone in the Earth's mantle. Nature 405:559–562
20. Tian Y, Hung SH, Nolet G, Montelli R, Dahlen FA (2007) Dynamic ray tracing and traveltime corrections for global seismic tomography. J Comput Phys 226:672–687
21. Lu C, Grand SP, Lai H, Garnero EJ (2019) TX2019slab: A new P and S tomography model incorporating subducting slabs. J Geophys Res 124(549–11):567
22. Ekström G, Nettles M (1997) Calibration of the HGLP seismograph network and centroid-moment tensor analysis of significant earthquakes of 1976. Phys Earth Planet Inter 101(3–4):219–243
23. Altamimi Z, Métivier L, Rebischung P, Collilieux X, Chanard K, Barnéoud J (2023) ITRF2020 plate motion model. Geophys Res Lett 50(24):7
24. Ringwood AE (1975) Composition and petrology of the Earth's mantle. McGraw-Hill, New-York 678
25. Flanagan M, Shearer P (1998) Topography on the 410-km seismic velocity discontinuity near subduction zones from stacking of sS, sP, and pP precursors. *J. Geophys. Res.* 103, 21,165– 21,182
26. Ito E, Takahashi E (1989) Postspinel transformations in the system Mg_2SiO_4-Fe_2SiO_4 and some geophysical implications. J Geophys Res 94:10637–10646

27. Vacher P, Mocquet A, Sotin C (1998) Computation of seismic profiles from mineral physics: The importance of the non-olivine components for explaining the 660 km depth discontinuity. Phys Earth Planet Inter 106:275–298
28. Connolly JAD (2005) Computation of phase equilibria by linear programming: A tool for geodynamic modeling and its application to subduction zone decarbonation. Earth Planet Sci Lett 236:524–541
29. Stixrude L, Lithgow-Bertelloni C (2011) Thermodynamics of mantle minerals—II. Phase equilibria. Geophys J Int 184(3):1180–1213
30. Maguire R, Ritsema R, Goes S (2018) Evidence of subduction-related thermal and compositional heterogeneity below the United States from transition zone receiver functions. Geophys Res Lett 45:8913–8922
31. Feng J, Yao H, Wang Y, Poli P, Mao Z (2021) Segregated oceanic crust trapped at the bottom mantle transition zone revealed from ambient noise interferometry. Nat Commun 12:2531
32. Yang X, Xie Y, Rychert CA, Harmon N, Goes S, Rietbrock A, Lynch L (2025) Members of the VoiLA Working Group. Seismic imaging of a basaltic Lesser Antilles slab from ancient tectonics. Nature 640:697–701
33. Karato SI, Riedel MR, Yuen DA (2001) Rheological structure and deformation of subducted slabs in the mantle transition zone: implications for mantle circulation and deep earthquakes. Phys Earth Planet Inter 127:83–108
34. Cross AJ, Goddard RM, Kumamoto KM, Goldsby DL, Hansen LN, Chen H, Hein D, Thom CA, Nehring MA, Breithaupt T, Wallis D (2025) Direct observations of transient weakening during phase transformations in quartz and olivine. Nat Geosci 18:548–554
35. Hu J, Gurnis M, Rudi J, Stadler G, Müller RD (2022) Dynamics of the abrupt change in Pacific plate motion around 50 million years ago. Nat Geosci 15
36. Ghosh S, Ohtani E, Litasov KD, Suzuki A, Dobson D, Funakoshi K (2013) Effect of water in depleted mantle on post-spinel transition and implication for 660 km seismic discontinuity. Earth Planet Sci Lett 371–372:103–111
37. Li J, Wang X, Wang XJ, Yuen DA (2013) P and SH velocity structure in the upper mantle beneath Northeast China: evidence for a stagnant slab in hydrous mantle transition zone. Earth Planet Sci Lett 367:71–81
38. Kelbert A, Schultz A, Egbert G (2009) Global electromagnetic induction constraints on transition-zone water content variations. Nature 460:1003–1006
39. Higo Y, Inoue T, Irifune T, Yurimoto H (2001) Effect of water on the spinel–postspinel transformation in Mg_2SiO_4. Geophys Res Lett 28:3505–3508
40. Katayama I, Hirose K, Yurimoto H, Nakashima S (2003) Water solubility in majoritic garnet in subduction oceanic crust. Geophys Res Lett 30. 10.1029/2003GL018127
41. Bercovici D, Karato S (2003) Whole-mantle convection and the transition-zone water filter. Nature 425:39–44
42. Kohlstedt DL, Keppler H, Rubie DC (1996) Solubility of water in the α, β, and γ phases of $(Mg,Fe)_2SiO_4$. Contrib Mineral Petrol 123:345–357

43. Bolfan-Casanova N, Keppler H, Rubie DC (2003) Water partitioning at 660 km depth and evidence for very low water solubility in magnesium silicate perovskite. Geophys Res Lett 30. 10.1029/2003GL017182
44. Kuritani T, Ohtani E, Kimura J (2011) Intensive hydration of the mantle transition zone beneath China caused by ancient slab stagnation. Nat Geosci 4:713–716
45. Faccenna C, Holt AF, Becker TW, Lallemand S, Royden LH, Royden (2018) Dynamics of the Ryukyu/Izu-Bonin-Marianas double subduction system. Tectonophysics 746:229–238
46. Shi D, Shen Y, Zhao W, Li A (2009) Seismic evidence for a Moho offset and south-directed thrust at the easternmost Qaidam-Kunlun boundary in the Northeast Tibetan plateau. Earth Planet Sci Lett 288:329–334
47. Ligorria J, Ammon CJ (1999) Iterative deconvolution and receiver function estimation. Bull Seismol Soc Am 89:1395–1400
48. Xu W, Lithgow-Bertelloni C, Stixrude L, Ritsema J (2008) The effect of bulk composition and temperature on mantle seismic structure. Earth Planet Sci Lett 275:70–79
49. Amaru M (2007) Global Travel Time Tomography with 3-D Reference Models. Utrecht Univ
50. Rudolph ML, Lekić V (2015) Lithgow-Bertelloni, C. Viscosity jump in Earth's mid-mantle. Science 350:1349–1352
51. Methods
52. Seismic data and construction of receiver-function cross-sections
53. Seismic data for this study were collected from broadband seismic stations in China and adjacent regions, including permanent stations from the China Earthquake Administration (*doi:10.11998/SeisDmc/SN,doi*:10.12001*/ChinArray.Data.Himalaya)*, temporary stations from NECsaids (the Northeast China Seismic Array to Investigate Deep Subduction), NECESSArray (the Northeast China Extended Seisimc Array)[16], and NETS (NorthEastern Tibet Seismic) experiments[46]
54. We processed waveform data from teleseismic events with magnitudes larger than 5.0 and epicentral distances ranging from 30 to 90º. We used the time-domain iterative deconvolution technique[47] in the calculation of the RFs, in which the Gaussian filter factor was set to 2 to suppress high-frequency(≥ 1 Hz) noise. We visually examined all the waveform data, corrected the sensor misorientation and discarded the data with abnormal waveform and low coherence. We finally obtained a total of 65655 high-quality RFs from 1339 seismic stations
55. The seismic cross -sections were obtained by projecting and stacking all the RFs within 1° distance from the cross-sections onto the vertical plane for the cross-sections. All the cross-sections have a bin size of 25 km × 0.5 km respectively along the cross-section and the depth directions
56. Mineral physics modeling and simulation of abnormally depressed post-spinel phase transition
57. We computed the effects of temperature and composition on mineral phase equilibria, and the depth variation of seismic velocities and densities with the Perple X code[28] and the elastic parameter database of ref. 29. We consider the subducted slab to be either an equilibrium assemblage (EA) or a mechanical mixture (MM) of basalt (i.e., oceanic crust) and harzburgite (i.e., oceanic mantle lithosphere). The mechanical mixture is a good approximation when the re-equilibration rate of basalt

and harzburgite in the slab is considered to be slow[48], and more convenient to be used for comparison under the first-order approximation. The end member compositions basalt and harzburgite are from ref. 48 (see Extended data Table 1)

58. Based on thermodynamic relations water incorporation into ringwoodite can expand its stability field to higher pressures relative to anhydrous system[2]. We modeled such delays in the phase transitions by shifting the relevant velocity and density curves downwards by the corresponding depths, irrespective of which minor element indeed caused the additional (or excess) depression of the discontinuity. The effects of adiabatic thermal expansion with depth, derived from the additional depression, are ignored, because they are secondary to the effects of the phase change

Methods

Seismic data and construction of receiver-function cross-sections

Seismic data for this study were collected from broadband seismic stations in China and adjacent regions, including permanent stations from the China Earthquake Administration (*doi:10.11998/SeisDmc/SN,doi:10.12001/ChinArray.Data.Himalaya*), temporary stations from NECsaids (the Northeast China Seismic Array to Investigate Deep Subduction), NECESSArray (the Northeast China Extended Seisimc Array)[16], and NETS (NorthEastern Tibet Seismic) experiments[46].

We processed waveform data from teleseismic events with magnitudes larger than 5.0 and epicentral distances ranging from 30 to 90°. We used the time-domain iterative deconvolution technique[47] in the calculation of the RFs, in which the Gaussian filter factor was set to 2 to suppress high-frequency(≥1 Hz) noise. We visually examined all the waveform data, corrected the sensor misorientation and discarded the data with abnormal waveform and low coherence. We finally obtained a total of 65655 high-quality RFs from 1339 seismic stations.

The seismic cross-sections were obtained by projecting and stacking all the RFs within 1° distance from the cross-sections onto the vertical plane for the cross-sections. All the cross-sections have a bin size of 25 km ´ 0.5 km respectively along the cross-section and the depth directions.

Mineral physics modeling and simulation of abnormally depressed post-spinel phase transition

We computed the effects of temperature and composition on mineral phase equilibria, and the depth variation of seismic velocities and densities with the Perple X code[28] and the elastic parameter database of ref. 29. We consider the subducted slab to be either an equilibrium assemblage (EA) or a mechanical mixture (MM)of basalt (i.e., oceanic crust) and harzburgite (i.e., oceanic mantle lithosphere). The mechanical mixture is a good approximation when the re-equilibration rate of basalt and harzburgite in the slab is considered to be slow[48], and more convenient to be used for comparison under the first-order approximation. The end member compositions basalt and harzburgite are from ref.48(see Extended data Table 1).

Based on thermodynamic relations, water incorporation into ringwoodite can expand its stability field to higher pressures relative to anhydrous system[2]. We modeled such delays in the phase transitions by shifting the relevant velocity and density curves downwards by the corresponding depths, irrespective of which minor element indeed caused the additional (or excess) depression of the discontinuity. The effects of adiabatic thermal expansion with depth, derived from the additional depression, are ignored, because they are secondary to the effects of the phase change.

Figures

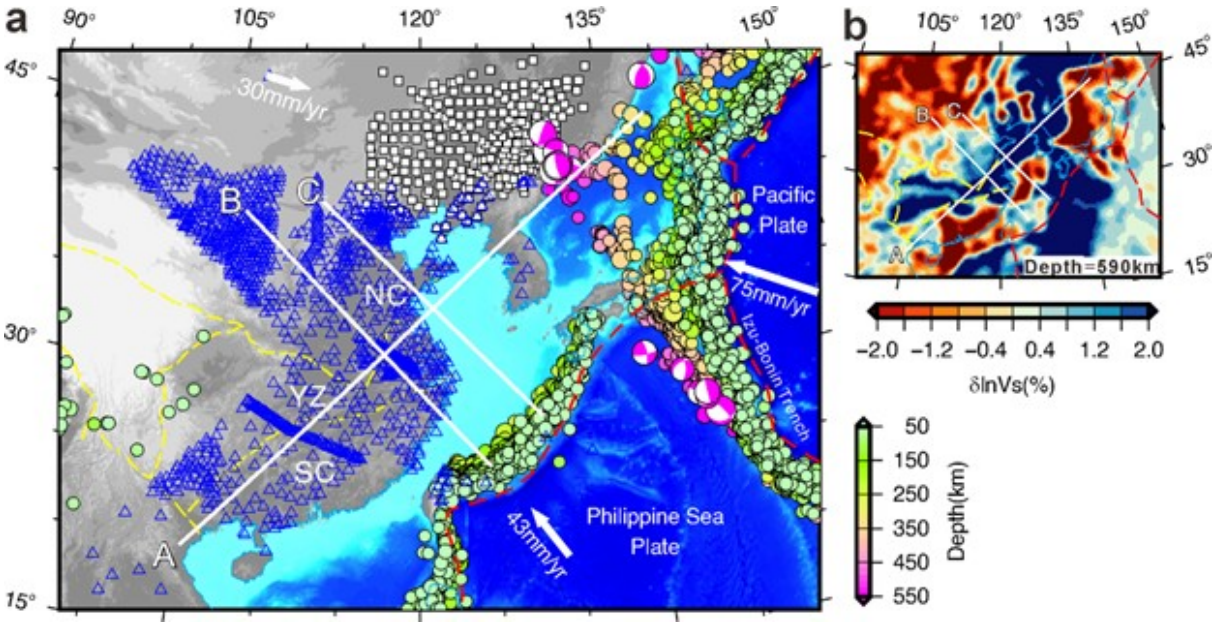

Figure 1

Plate tectonic setting and seismic stations used in the construction of the seismic cross-sections. a, Blue triangles denote the seismic stations processed in this study, and the white squares denote the seismic stations from the NECsaids and NECESS arrays[16]. White lines show the locations of the seismic cross-sections presented in Fig. 2. Solid color circles show the distribution with the depth of the seismicity with magnitudes≥4.5 since January 2001 from the USGS catalog, depicting the slab geometry of the modern Pacific and Philippine Sea plates in the region. The purple–white quadrant circles show the focal mechanisms[22] of earthquakes with depths≥500 km since January 1976. Red and yellow dashed lines show modern and ancient plate boundaries. White arrows denote the modern plate motions in the plate International Terrestrial Reference Frame (ITRF2020)[23]. **b,** The tomographic image of the stagnant slabs (featured by bluish velocity anomalies) in the MTZ in the full-waveform S-wave tomographic model FWEA23[17]. NC, North China; YZ, Yangtze; SC, South China.

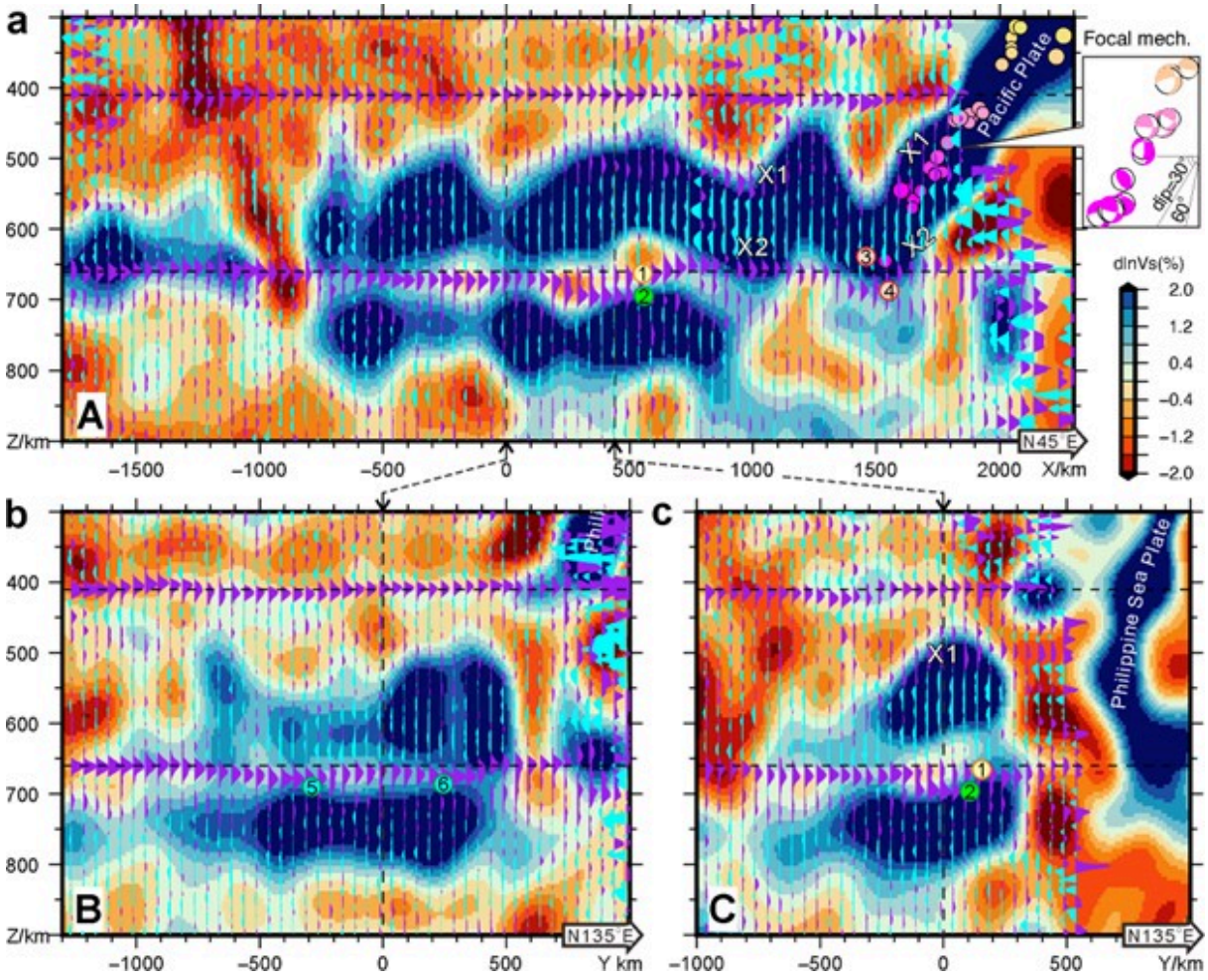

Figure 2

Receiver function cross-sections of the MTZ structure across the stagnant slabs in the study region. Positive and negative converted phases are plotted in purple and cyan, representing interfaces with increasing and decreasing impedance with depth, respectively. Background shows the S-wave tomographic images of model FWEA23[17]. Focal mechanisms of earthquakes within a distance of 1º are projected onto the cross-sections. All the coordinates are referred to 117.5ºE, 32ºN and sea level. Dashed black lines at 410 and 660 km depths are for reference. The crossing points of the cross-sections are indicated by black arrows. For legibility, vertical scales are exaggerated by a factor of 2.85. Nomogram in the up-right panel shows appearance of true dips of 30° and 60° after the same vertical exaggeration.

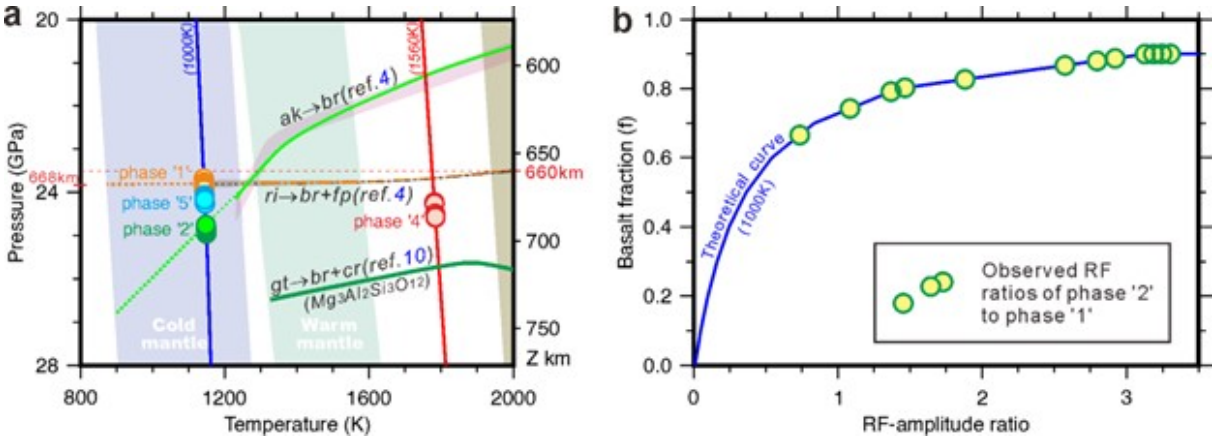

Figure 3

Predicted and observed depths and RF-amplitude ratios of the seismic phases. a, Phase transitions near 660 km depth predicted by recent in situ X-ray diffraction studies[4,9]. Color-filled circles show the depths observed for phases '1', '2', '5' and '4', plotted on the 1000K and 1560K mantle adiabats, respectively. **b,** Theoretical variations of RF-amplitude ratio of phase '2' to phase '1' with basalt fraction (f) along the 1000K mantle adiabat. Yellow filled circles are the ratios observed along profile A in Fig. 2. ak, akimotoite; br, bridgmanite; ri, ringwoodite; fp, ferropericlase; gt, garnet; cr, corundum.

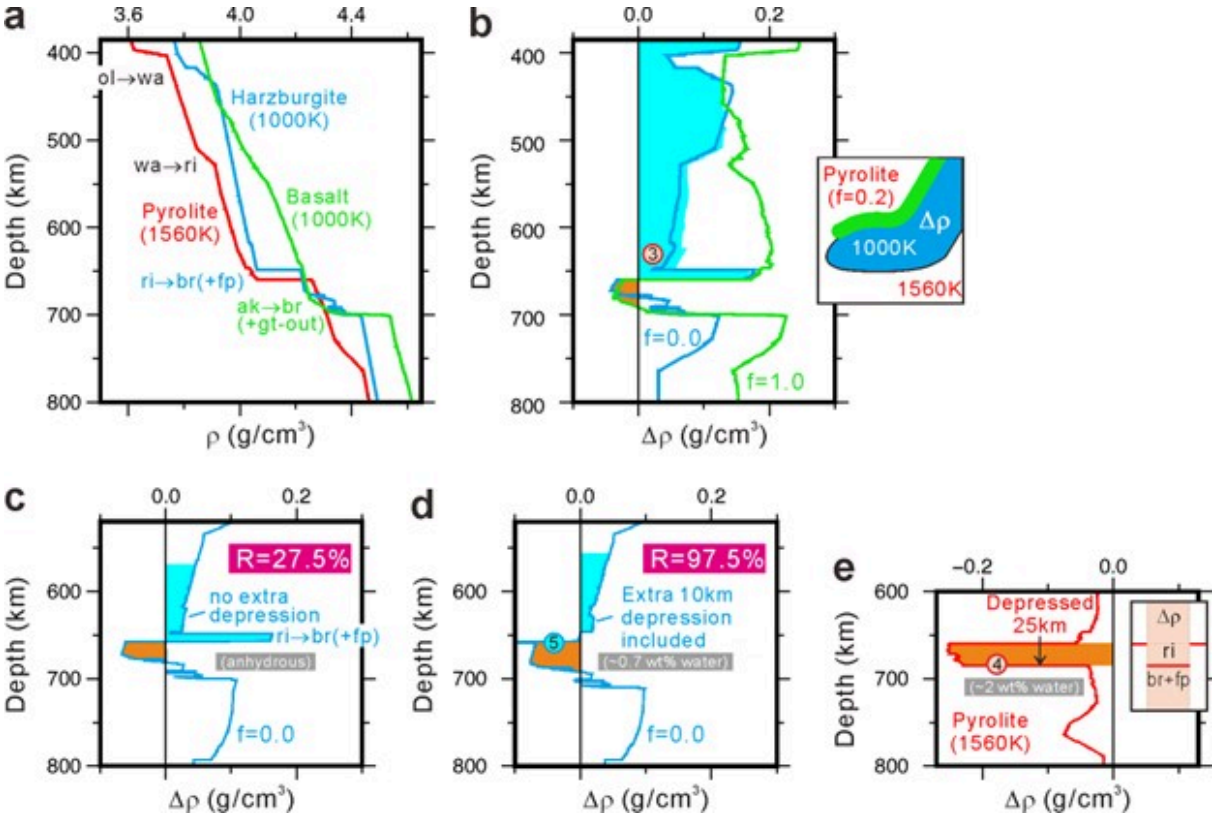

Figure 4

Theoretical densities (r) and density contrasts (Dr) for the stagnant slabs and surrounding mantle. a, Theoretical variations of densities with depth of the oceanic basalt crust (f=1.0; in green) and harzburgite

mantle lithosphere (f=0.0; in cyan) of the slabs and the pyrolitic surrounding mantle (f=0.2; in red), respectively along the 1000K and the 1560K mantle adiabats (cf. Extended data Fig. 5). **b,** Theoretical density contrasts of the basalt crust and harzburgite mantle lithosphere of the slabs with respect to the pyrolitic surrounding mantle. **c-d,** Theoretical density contrasts of the harzburgite slab with respect to the pyrolitic surrounding mantle, without and with an excess depression of 10 km in the phase transition, respectively. R stands for the ratio of the buoyancy to the negative buoyancy. **e,** Theoretical density contrasts derived from the depression of the post-spinel phase-transition in the pyrolitic surrounding mantle. Brown and cyan shaded areas are approximately proportional to the upward and downward buoyancies. ol, olivine; wa, wadleyite. Other annotations as in Fig. 3.

Supplementary Files

This is a list of supplementary files associated with this preprint. Click to download.

- ShietalRFs20250830SI.docx